Boosting Efficiency and Stability of Planar Inverted $(FAPbI_3)_x(MAPbBr_3)_{1-x}$ Solar Cells via $FAPbI_3$ and $MAPbBr_3$ Crystal Powders

Jiantao Wang, Fanxu Meng, Ruxue Li, Shaoqing Chen, Xiaoyu Huang, Jing Xu, Xiaosong Lin, Rui Chen, Hongkai Wu, and Hsing-Lin Wang*

Solution-processed perovskite precursors, especially for $MAPbBr_3$-assisted $FAPbI_3$ crystallization, has been noted to achieve high power conversion efficiency (PCE) for perovskite solar cells (PSCs). However, this low-temperature processed $(FAPbI_3)_x(MAPbBr_3)_{1-x}$ typical precursor derived from commercial products (FAI, PbI_2, MABr, and $PbBr_2$) suffers from environmental sensitivity, poor film crystallinity and less than ideal device reproducibility. Herein, $(FAPbI_3)_x(MAPbBr_3)_{1-x}$ $(0.80 \leq x \leq 0.90)$-based planar inverted PSCs are fabricated, employing grinded monocrystalline $MAPbBr_3$ and powdered polycrystalline $FAPbI_3$ as precursors. The champion device with optimal molar ratio $x = 0.85$ comprising highly crystalline larger-grained perovskite film with enhanced carrier transport kinetics and reduced trap-state density exhibits boosted efficiency reaching 20.50%, which shows a 22.90% improvement over typical precursors with a PCE of 16.68%. In addition, the crystal powder precursor yields obvious film stability under ambient conditions (23 °C, 65–85% humidity) for 150 days and improved device storage stability in the glove box within two months. This protocol using stock crystal powders for perovskite precursor formulation provides a relatively facile and reproducible device fabrication route for the commercialization of PSCs.

Organic lead halide perovskite has emerged as a class of star semiconducting materials for photovoltaic devices due to their thrilling power conversion efficiency (PCE) and solution-based low-cost device-processing technology.[1] Among them, $FAPbI_3$ has boosted the performance of perovskite solar cells (PSCs) to a higher level (over 20%) via compositional engineering, crystal

formation and grain boundary or interface passivation.[2–5] The aforementioned high-performance perovskite devices are resulting from mixing a small amount of cesium (Cs)/methylammonium (MA) lead halide into $FAPbI_3$ precursor to stabilize photoactive black phase α-$FAPbI_3$.[6,7] Recently, $MAPbBr_3$ or $MAPbI_3$-doped $FAPbI_3$ precursor with narrow bandgap have successively updated the highest reported PCE record in mesoporous and planar configuration.[5,8] However, this MAFA mixed precursor derived from commercial raw materials (FAI, PbI_2, MABr, and $PbBr_2$) suffers from environmental sensitivity, poor film crystallinity, and most of all, less-than-ideal device reproducibility.[6,9] Therefore, it remains a great challenge to mitigate the aforementioned drawbacks by low temperature (≤ 100 °C) processing method.

In recent years, precursor engineering is one of the most popular ways to form perovskite films with low trap density and high conversion efficiency.[10] Highly pure precursors using as-synthesized single crystal/powders instead of expensive commercial raw materials is a cost-effective method to prepare low-defect perovskite films with well-defined stoichiometry.[11–13] Previously, it is reported using perovskite single-crystal $MAPbX_3$ ($X = I$, Br, Cl) derived precursor yields highly crystalline thin film.[14] Powdered polycrystalline $MAPbI_3$-based precursors have been demonstrated to reduce interfacial trap density and enable 16.8% PCE with lower device hysteresis.[15] In addition, using solution-synthesized $MAPbI_{3-x}Cl_x$ perovskite powders as precursor has a reproducible PCE as high as 19.1%.[16] Recently, perovskite films processed by polycrystalline δ-$FAPbI_3$ crystal powders exhibited a 17.94% PCE after embodied in regular (n-i-p) PSCs.[12] Furthermore, one-pot synthesized $(FAPbI_3)_x(MAPbBr_3)_{1-x}$ single microcrystal as precursor has been studied to enhance crystallinity when processing films comparing with raw materials, leading to 18.3% PCE and long-term stability for regular devices.[17] Moreover, a high phase-purity α-$FAPbI_3$ films were obtained using presynthesized powder or single-crystal δ-$FAPbI_3$ with MACl additive and the corresponding regular-device PCEs were certified as 21.07% and 23.48%, respectively.[13] Despite recent success

J. Wang, Dr. F. Meng, Dr. S. Chen, X. Huang, J. Xu, X. Lin, Prof. H.-L. Wang
Department of Materials Science and Engineering
Southern University of Science and Technology
1088 Xueyuan Avenue, Shenzhen 518055, P. R. China
E-mail: wangxl3@sustech.edu.cn

J. Wang, Prof. H. Wu
Department of Chemistry
Hong Kong University of Science and Technology
Clear Water Bay Road, Hong Kong S.A.D., P. R. China

Dr. R. Li, Prof. R. Chen
Department of Electrical and Electronic Engineering
Southern University of Science and Technology
1088 Xueyuan Avenue, Shenzhen 518055, P. R. China

The ORCID identification number(s) for the author(s) of this article can be found under https://doi.org/10.1002/solr.202000091.

in achieving high efficiency and stability using synthesized crystal powders instead of commercial products in regular devices, only very limited works clarified impressively boosted performance (>20% PCE) for planar inverted (p-i-n) PSCs.[18] It is worth mentioning that planar inverted PSCs with light absorber sandwiched by low-temperature solution-processed organic hole and electron transporting layers are more likely to be commercialized in exible and tandem devices.

In this work, $MAPbBr_3$ single crystal and $FAPbI_3$ crystal powders were synthesized, and then both stock components were mixed with different molar ratios to prepare $(FAPbI_3)_x(MAPbBr_3)_{1-x}$ ($0.80 \leq x \leq 0.90$) precursor solutions. These solutions were processed to fabricate our standard devices with planar inverted configuration ITO/Poly(triarylamine) (PTAA)/perovskite/$PC_{61}BM$/Zirconium (IV) Acetylacetonate (ZrAcac)/Silver (Ag). We gained the best device with up to 20.50% PCE (optimal $x = 0.85$), a 22.90% improvement over the corresponding typical four component (FAI, PbI_2, MABr, and $PbBr_2$) precursor that has the highest PCE of 16.68%. It is revealed that this crystal powder precursor (CP) processed highly crystalline film with large grains exhibits enhanced carrier transport kinetics, reduced trap-state density and superior environmental stability thus boosting the reproducible performance of PSCs.

Figure 1a exhibits the synthesis of polycrystalline δ-$FAPbI_3$ and single-crystal $MAPbBr_3$ and the preparation of $(FAPbI_3)_x(MAPbBr_3)_{1-x}$ perovskite precursors. The optical images and X-ray diffraction (XRD) patterns of powders are shown in Figure S1, Supporting Information, in which the characteristic peak of $MAPbBr_3$ at 15.01° and nonperovskite phase δ-$FAPbI_3$ at 11.58° are consistent with the values of reported literatures.[19] To prepare precursor solutions, we weighed the stock crystal powders δ-$FAPbI_3$ and $MAPbBr_3$ with molar ratio x equaling to 0.80, 0.83, 0.85, 0.87, and 0.90. This molar ratio range is noted for perovskite crystallization with low-temperature (≤ 100 °C) solution process, especially, when x equals to 0.83 or

0.85.[2,7] The deposition of perovskite films, as shown in Figure 1b, were performed following one-step antisolvent method.[20] After chlorobenzene (CB) treatment at 10 s before the end of the high-speed spin-coating process and straightway 100 °C annealing for 30 min, δ-$FAPbI_3$ is converted into photoactive α-$FAPbI_3$ that has the characteristic XRD peak at 14.01° as shown in Figure S2, Supporting Information; however, the conversion is not complete until the doping ratio of $MAPbBr_3$ is over 15%. UV–vis absorption curves of fabricated thin films are plotted in Figure S3, Supporting Information. The absorption onset edge shifts about 25 nm to near infrared region when increasing the molar ratio of δ-$FAPbI_3$ from 0.80 to 0.90, which suggests that the increased overall ratio of $FAPbI_3$ is responsible for the improved light-harvesting ability of perovskite films. In addition, the red shift also confirmed from photoluminescence (PL) spectra shown in Figure S4, Supporting Information, reveals that the optical bandgap of perovskite thin films becomes narrower once adding less $MAPbBr_3$ into $FAPbI_3$.

As planar inverted PSCs own intrinsic advantages of straightforward fabrication, negligible hysteresis and fatigue behavior, we fabricated the planar inverted PSCs in which every layer was prepared via solution-processed spin-coating method except for the top contact silver electrode.[21] **Figure 2**a,b presents the device structure and scanning electron microscope (SEM) cross-section morphology of $(FAPbI_3)_{0.85}(MAPbBr_3)_{0.15}$ device. We opted a thin layer of dopant-free PTAA as hole transporting material (HTM) due to its excellent charge extraction and electron blocking ability.[22] The dependence of statistical device PCE on molar ratio is shown in Figure 2c. Figure S5, Supporting Information, exhibits the current density–voltage (J–V) curves of the champion devices with the change of x values, and the average device photovoltaic parameters are listed in Table S1, Supporting Information. By comparison, it is noteworthy that the average PCE is highly enhanced when the molar ratio x equals to 0.85. When x moves toward 0.85, the photovoltaic performance of our best device reaches 20.50% PCE and the photovoltaic parameters are close
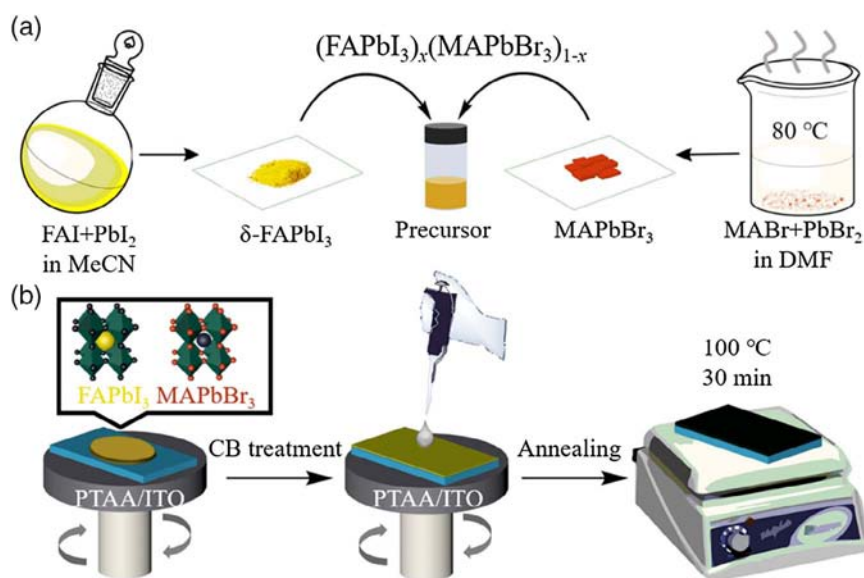

Figure 1. Schematic diagram illustrates a) the preparation of perovskite precursors and b) the fabrication process of perovskite films.
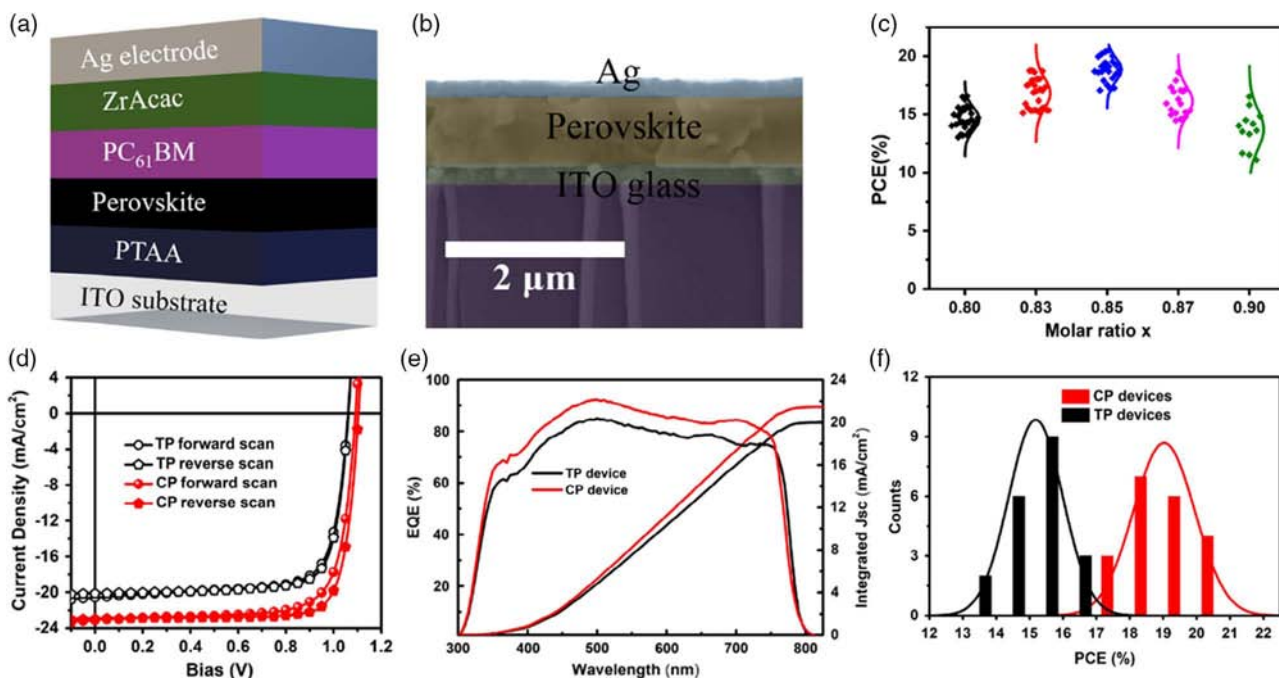
Figure 2. a) Device structure, b) SEM of device cross-section, c) PCE statistics of crystal powder derived $(FAPbI_3)_x(MAPbBr_3)_{1-x}$ PSCs. d) J–V curves, e) EQE and integrated J_{sc}, and f) PCE histogram of CP and TP-derived $(FAPbI_3)_{0.85}(MAPbBr_3)_{0.15}$ devices.

to their max values with the open-circuit voltage (V_{oc}) of 1.10 V, the short-circuit current density (J_{sc}) of 22.99 mA cm^{-2}, and the fill factor (FF) of 80.77%. Figure S6, Supporting Information, gives a report of the external quantum efficiency (EQE) and the integrated J_{sc} curves. The arrangement of EQE infrared edges is consistent with the film absorption spectra in Figure S3, Supporting Information, proving that the increasing proportion of FAPbI$_3$ contributes the narrower bandgap, leading to redshifts of light absorption edge. However, the film crystallization depends on the doping molar ratio of MAPbBr$_3$ according to the XRD patterns in Figure S2, Supporting Information. It implies that $(FAPbI_3)_{0.85}(MAPbBr_3)_{0.15}$ PSC with good crystallization and relatively narrow bandgap gains the best performance with highest integrated J_{sc} 21.42 mA cm^{-2}. This optimal molar ratio $x = 0.85$ is highly consistent with the devices derived from commercial products (FAI, PbI$_2$, MABr, and PbBr$_2$).[2] It is noteworthy that the reported powder-based works with the highest efficiency (over 22%) used the mixed composition of $(FAPbI_3)_{0.95}(MAPbBr_3)_{0.05}$ under 150 °C postannealing process.[5,23] We also checked this composition by 150 °C heating instead of 100 °C to prepare perovskite films and fabricated planar inverted PSCs. However, the film XRD (Figure S7, Supporting Information) showed that it did not fully convert into perovskite, and we only obtained a highest device PCE of 12.86% with a V_{oc} of 0.88 V, a J_{sc} of 19.62 mA cm^{-2}, and 74.73% FF measured by the reverse scan, whereas the forward scan PCE 10.84%, with a V_{oc} of 0.76 V, a J_{sc} of 19.59 mA cm^{-2}, and 73.06% FF, as shown in Figure S8, Supporting Information. Poor crystallinity and excess migrated ions probably lead to poor device performance and noticeable hysteresis. Considering the advantage of narrower bandgap when $x = 0.95$, more detailed work such as solvent composition and

additive engineering show potential to achieve better performance of PSCs.

Next, we compared $(FAPbI_3)_{0.85}(MAPbBr_3)_{0.15}$ perovskite photovoltaic devices fabricated from CP and four-component typical precursor (namely TP). The J–V curves of both best-performed devices has been plotted in Figure 2d. The highest PCE of aforementioned CP device is 20.50%. This is an improvement of 22.90% over the TP champion device that has a PCE of 16.68%, with a V_{oc} of 1.06 V, a J_{sc} of 20.12 mA cm^{-2}, and an FF of 78.05%, as listed in **Table 1**. Their current density values calculated from EQE are 19.97 and 21.42 mA cm^{-2} for TP and CP devices, respectively, as shown in Figure 2e, which are well consistent with the J_{sc} difference. The PCE histogram of 20 devices is shown in Figure 2f where CP devices all harvest over 17% PCE, reproducibly higher than TP devices.

To better understand the superiority of this grinded monocrystalline MAPbBr$_3$ and powdered polycrystalline FAPbI$_3$ mixed precursor, we first perform control experiment by preparing corresponding CP and TP perovskite films. Following the same spin-coating procedure and 100 °C annealing, both resulted brown films transform into shiny-dark planar surface

Table 1. Photovoltaic parameters of best device from CP and TP precursor.

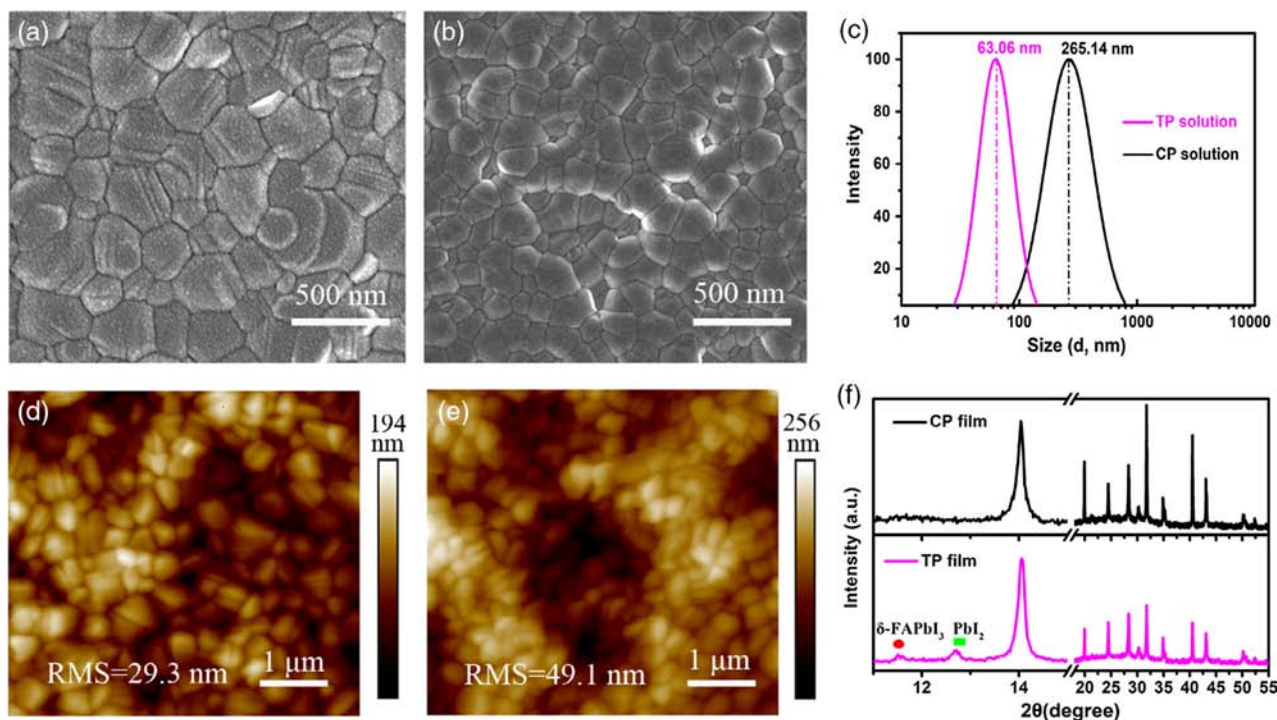| Precursor		V_{oc} [V]		J_{sc} [mA cm^{-2}]		FF [%]		PCE [%]	
CP	Average	1.10	0.01	22.22	0.59	78.09	2.67	19.03	0.89
	Best	1.10		22.99		80.77		20.50	
TP	Average	1.03	0.05	19.38	0.81	76.46	1.77	15.18	0.75
	Best	1.06		20.12		78.05		16.68	

Figure 3. SEM and XRD of a,d) CP and b,e) TP film. c) DLS and f) XRD of CP and TP.

with no obvious distinction. However, under SEM, we found the top surface morphology of CP film yields uniform larger grains with pinhole-free coverage as shown in **Figure 3**a, whereas the TP film presents relatively small grains (Figure 3b). We believe the difference in film morphology is related to the crystallization process where the discrepancy of precursor solution such as species purity, stoichiometry, and colloidal sizes dictates the film quality and final device performance.[24] First and foremost, the as-synthesized monocrystalline MAPbBr$_3$ and polycrystalline FAPbI$_3$-derived CP should have more accurate MABr/PbBr$_2$ and FAI/PbI$_2$ mole ratio in 1:1 stoichiometry than TP due to the impurity in commercial products. In addition, the subtle metal or transition metal impurities and the fractional deviations in TP stoichiometry may have an adverse impact on the colloid size. We assume the main chemical species such as MA$^+$, FA$^+$, Pb^{2+}, I$^-$, and Br$^-$ are the same, but the stoichiometry of individual components and their interaction with impurities in TP solution may lead to a smaller colloidal size which plays a significant role in crystal growth of unsaturated solutions.[25] We then measured the colloidal sizes of both precursors solution with precise 1 h aging time using dynamics light scattering (DLS). The CP solution has a nuclei size of 265.14 nm, whereas the TP solution obtains as small as 63.06 nm, as shown in Figure 3c. It is revealed that the larger nuclei size and smaller number of nucleation sites after sprinkling the antisolvent, result in the formation of larger crystal grains.[26] The topographies of perovskite films deposited on PTAA substrates were measured by atomic force microscope (AFM) with a larger scale of 5 × 5 m^2. As shown in Figure 3d,e, both CP and TP perovskite films have dense and pinhole-free coverage. AFM results also show that CP film

presents a larger grain-size morphology, and its root mean square (RMS) roughness of 29.3 nm is smaller than TP film of 49.1 nm, exhibiting a smoother top-surface morphology. XRD of both films is shown in Figure 3f; we have observed obvious δ-FAPbI$_3$ peaks at 11.58° and PbI$_2$ at 12.8° of TP film, which suggests that the precursor solution derived from TP commercial products leads to a decreased crystallinity and phase purity of perovskite films. Such residual PbI$_2$ impurity in films may act as a passivation reagent for grain boundaries or interfaces between perovskite and transporting layers, which results in less hysteresis of TP device as shown in Figure 2d.[27] This result also suggests that further enhanced performance for CP devices can be expected by applying a suitable passivating layer.

The scanning Kelvin probes microscopy (SKPM) as a general and facial method was then performed to study the electronic chemical potential of perovskite films.[28] Surface potential of CP and TP films are defined as shown in **Figure 4**a,b. The line-cut profiles extracted from the measured SKPM image are shown in Figure S9, Supporting Information, where −369.08 ± 10.06 mV for CP/PTAA film and −301.27 ± 9.02 mV for TP/PTAA film. A bigger absolute surface potential value of CP film, ≈70 mV more than TP film, signifies a stronger charge extraction effect of PTAA when contacting CP film.[29] To analyze the charge carrier kinetics, we characterized the optical properties of both films prepared on PTAA substrates and quartzes respectively (Figure 4c). These four samples have a steady-state PL at 790 nm under 455 nm excitation, and the emission was quenched when the perovskite films were deposited on PTAA substrates due to the fast charge transfer to HTM.[30] The PL intensity of CP film on quartz > TP film on quartz > TP film on PTAA/ITO substrate > CP film on PTAA/ITO substrate suggests less perovskite bulk defects due
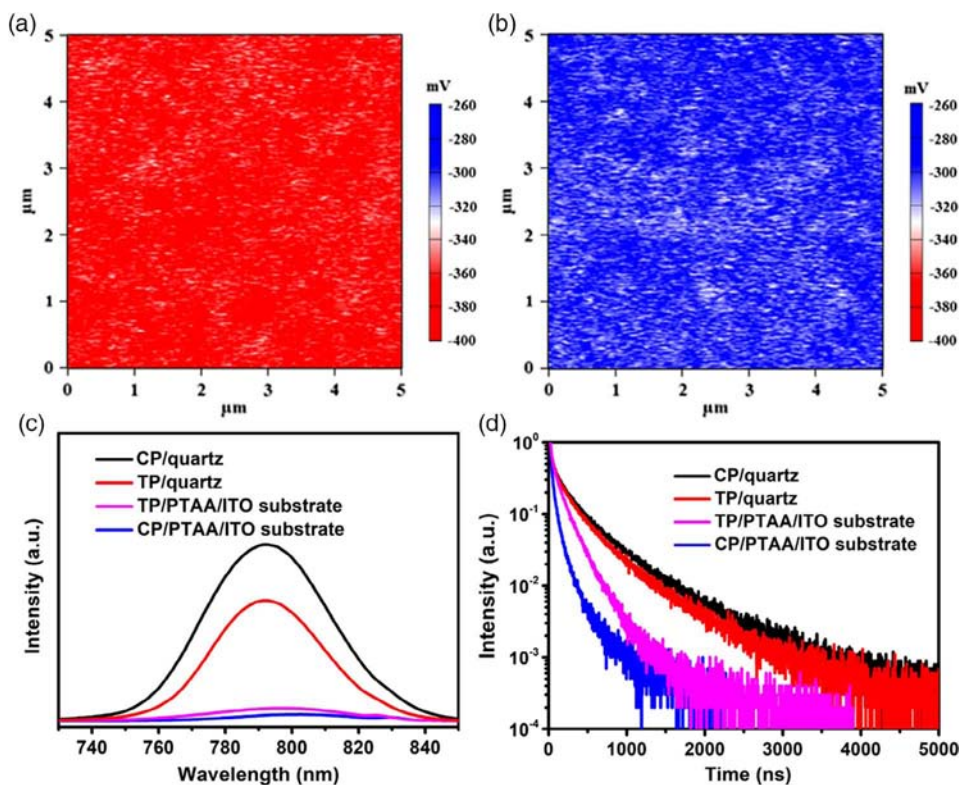
Figure 4. SKPM of a) CP and b) TP films. c) PL and d) TRPL of CP and TP films.

to high purity, better film crystallinity, and faster carrier transport from CP film to PTAA HTM compared with TP film. To further verify the photogenerated charge transfer kinetics between perovskite and PTAA, we measured the time-resolved PL (TRPL) of TP and CP films formed on quartzes and PTAA substrates. Figure 4d shows the decay profiles of the aforementiioned four films, where the average decay lifetimes (τ_{av}) of CP and TP films deposited on quartzes are determined to be 423.86 and 351.97 ns, respectively, and those deposited on PTAA substrates are 85.62 and 159.66 ns, respectively. The τ_{av} value of CP bulk film is longer than TP film, which could be attributed to the high quality of the bulk perovskite. In addition, the decay of CP/PTAA drops faster than TP/PTAA signifies a rather more rapid loss of CP film carriers extracted by PTAA and/or interfacial recombination and this most probably benefited from its larger grain coverage and less grain boundaries.[31] From the aforementioned results, we have concluded that the perovskite films processed from crystal powder has led to superior morphological and electronic properties such as larger grain size, lower defects, and boosted carrier transport kinetics.

The statistic distributions of the photovoltaic parameters V_{oc}, J_{sc}, and FF were in-depth analyzed as shown in Figure S10, Supporting Information. For J_{sc} and FF, both are related to the grain size of perovskite films. The large-grained thin film with fewer defects, suppressed charge trapping, and higher charge transport kinetics leads to a higher current density average J_{sc} 22.22 mA cm^{-2} and FF 78.09% for CP precursor devices, whereas the TP devices have a lower current density average J_{sc} 19.38 mA cm^{-2} and FF 76.46%.[4,25] Moreover, it is important to note that the V_{oc} of CP devices with average 1.10 V is higher and narrower distributed than TP devices with average 1.03 V. The V_{oc} loss of 70 mV could be attributed to the decreased trap-assisted recombination of charge carrier in bulk perovskite and interfaces. To characterize the trap-state density, we fabricated electron-only devices of ITO/SnO$_2$/Perovskite/PC$_{61}$BM/Zracac/Ag and obtained the space-charge-limited conduction (SCLC) with the change of CP and TP perovskite films. From the dark J–V curves as shown in Figure S11, Supporting Information, the trap-filled limited voltage (V_{TFL}) can be read from the intersection of linear fits of ohmic regime and SCLC regime.[32] According to the equation $V_{TFL} = eN_t d^2 / 2\varepsilon_r\varepsilon_0$, where e is the charge constant, N_t is the electron trap-state density, d is the thickness of perovskite film, ε_r is the relative dielectric constant, ε_0 is the vacuum permittivity; the decreased V_{TFL} from 0.22 V of TP to 0.14 V of CP is determined by the corresponding N_t from 5.64 $\times$ 10^{15} cm^{-3} to 3.59 $\times$ 10^{15} cm^{-3}.[33] The lower trap-state density of CP contributes a suppressed nonradiative recombination. To give a comparison of recombination process along the entire pathway during solar cells operation, we tested the J_{sc} and V_{oc} change in both devices as a function of light intensity.[34] Measured J_{sc} with the change in light intensity shows a linear correlation for TP and CP devices (Figure S12, Supporting Information), where the slope values are 0.98 and 1.01, respectively, inferring negligible radiative recombination in both working devices. As shown in **Figure 5**a, CP device has a slope of 1.219 K$_B$T q^{-1}, deviating less from K$_B$T q^{-1} than TP device of 1.437 K$_B$T q^{-1}, indicating a reduced trap-assisted nonradiative recombination. Inhibited
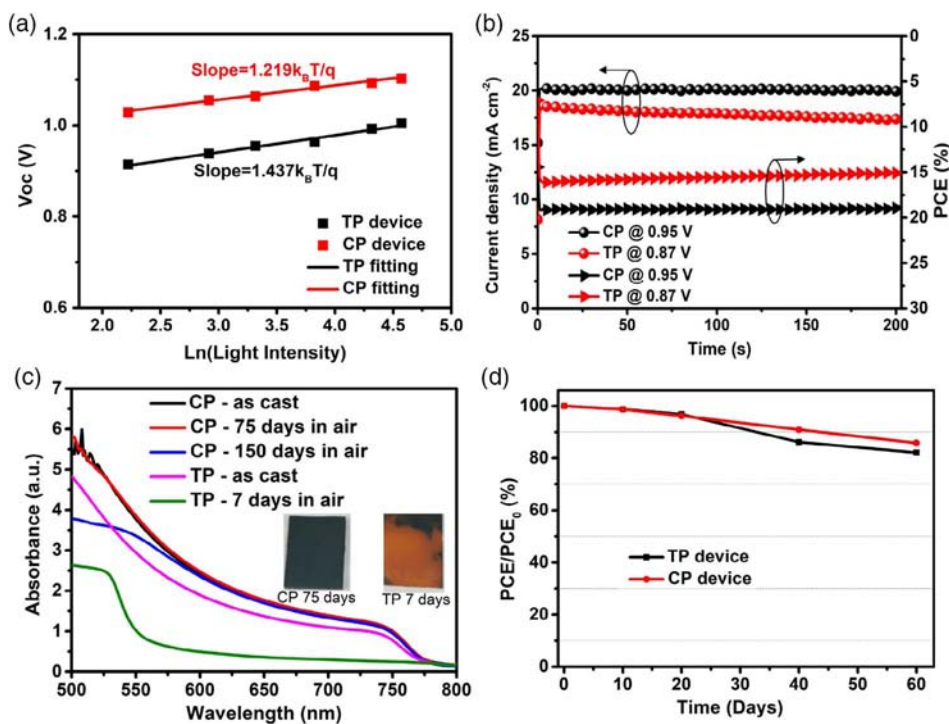
Figure 5. a) V_{oc} variation with the change of light intensity, b) MPP output, c) film stability in ambient condition, and d) device storage stability.

nonradiative recombination energy loss mediated by decreased trap-state density in CP device results in a higher V_{oc}, which is consistent with the PCE measurements.[35]

The stabilized outputs at the maximum power point (MPP) of a representative TP and CP device are plotted in Figure 5b. The slight downward trend of TP photocurrent density as a function of time compared to CP suggests a more stable MPP of CP device under $100 \, mW \, cm^{-2}$ AM 1.5G solar illumination. The output of PCE 19.16% and 16.11% for CP and TP, respectively, gives an accurate confirmation of PCE measurements, which fulfil the requirement of reproducibility. To study the environmental stability of the perovskite thin films, we compare UV–vis absorption of CP and TP films as a function of storage time at ambient condition ($23 \, °C$, 65–85% humidity), and the results are shown in Figure 5c. It is surprising to note that the CP film keeps stable without any change in 75 days as shown in the inset optical image of Figure 5c and only slight decline of absorbance from 575 nm after 150 days. However, as can be clearly seen, the TP film shows a nearly complete degradation within only one week as suggested by its absorption edge shift from 780 to 550 nm. The superior environmental stability of CP film was attributed to the high purity, improved crystallinity, large grained size and decreased grain boundary, which can effectively suppress oxygen and moisture-mediated degradation.[36] Finally, we measured the stability of CP- and TP-derived devices stored in glove box, and the results are shown in Figure 5d. Both devices reveal a similar trend in the first 20 days. However, the CP device exhibits better stability and can keep over 85% of the initial PCE after 2 months. Crystal-powder-based devices with a promoted stability is mainly resulting from improved crystallinity, higher phase purity, larger grained morphology, and environmental

stability of the perovskite films as manifested by SEM, XRD, SKPM, PL, and UV–vis spectra.[37]

In summary, we have achieved high-efficient planar inverted solar cells via grinded monocrystalline $MAPbBr_3$ and powdered polycrystalline $FAPbI_3$ as mixed cation perovskite precursors. The low-temperature-processed CP-derived $(FAPbI_3)_{0.85}(MAPbBr_3)_{0.15}$ PSCs with reproducible over 20% PCE exhibit superior performance than commercial products (FAI, PbI_2, MABr, and $PbBr_2$)-based precursor which was attributed to improved crystallinity, facilitated carrier transport, and reduced trap-assisted charge recombination. CP-based stable perovskite thin films possess larger grain size, as well as a dramatically improved device PCE, 22.90% more than the TP perovskite film, and promoted shelf storage stability. Our protocol using stock crystal powders for perovskite precursor formulation provides a facile and reproducible device fabrication route for the commercialization of PSCs.

Supporting Information

Supporting Information is available from the Wiley Online Library or from the author.

Acknowledgements

Conflict of Interest

The authors declare no conflict of interest.

Keywords

boosting performance, crystal powders, perovskite solar cells, planar inverted, stability

[1] a) H. S. Kim, C. R. Lee, J. H. Im, K. B. Lee, T. Moehl, A. Marchioro, S. J. Moon, R. Humphry-Baker, J. H. Yum, J. E. Moser, M. Gratzel, N. G. Park, *Sci. Rep.* **2012**, *2*, 591; b) V. D'Innocenzo, G. Grancini, M. J. P. Alcocer, A. R. S. Kandada, S. D. Stranks, M. M. Lee, G. Lanzani, H. J. Snaith, A. Petrozza, *Nat. Commun.* **2014**, *5*, 3586; c) Q. Dong, P. Mulligan, J. Qiu, Y. Fang, L. Cao, Y. Shao, P. J. Huang, *Science* **2015**, *347*, 967; d) K. X. Steirer, P. Schulz, G. Teeter, V. Stevanovic, M. Yang, K. Zhu, J. J. Berry, *ACS Energy Lett.* **2016**, *1*, 360; e) N. R. E. L., Best Research-Cell Efficiency Chart, https://www.nrel.gov/pv/assets/pdfs/best-research-cell-efficiencies-190416.pdf (accessed: August 2019); f) N. J. Jeon, J. H. Noh, Y. C. Kim, W. S. Yang, S. Ryu, S. I. Seok, *Nat. Mater.* **2014**, *13*, 897; g) J. Burschka, N. Pellet, S.-J. Moon, R. Humphry-Baker, P. Gao, M. K. Nazeeruddin, M. Grätzel, *Nature* **2013**, *499*, 316; h) Y. Zhong, R. Munir, J. Li, M.-C. Tang, M. R. Niazi, D.-M. Smilgies, K. Zhao, A. Amassian, *ACS Energy Lett.* **2018**, *3*, 1078.

[2] N. J. Jeon, J. H. Noh, W. S. Yang, Y. C. Kim, S. Ryu, J. Seo, S. I. Seok, *Nature* **2015**, *517*, 476.

[3] D. Bi, C. Yi, J. Luo, J.-D. Décoppet, F. Zhang, S. M. Zakeeruddin, X. Li, A. Hagfeldt, M. Grätzel, *Nat. Energy* **2016**, *1*, 1.

[4] W. Nie, H. Tsai, R. Asadpour, J.-C. Blancon, A. J. Neukirch, G. Gupta, J. J. Crochet, M. Chhowalla, S. Tretiak, M. A. Alam, H.-L. Wang, A. D. Mohite, *Science* **2015**, *347*, 522.

[5] E. H. Jung, N. J. Jeon, E. Y. Park, C. S. Moon, T. J. Shin, T. Y. Yang, J. H. Noh, J. Seo, *Nature* **2019**, *567*, 511.

[6] M. Saliba, T. Matsui, J. Y. Seo, K. Domanski, J. P. Correa-Baena, M. K. Nazeeruddin, S. M. Zakeeruddin, W. Tress, A. Abate, A. Hagfeldt, M. Gratzel, *Energy Environ. Sci.* **2016**, *9*, 1989.

[7] W. S. Yang, J. H. Noh, N. J. Jeon, Y. C. Kim, S. Ryu, J. Seo, S. I. Seok, *Science* **2015**, *348*, 1234.

[8] Q. Jiang, Y. Zhao, X. Zhang, X. Yang, Y. Chen, Z. Chu, Q. Ye, X. Li, Z. Yin, J. You, *Nat. Photonics* **2019**, *13*, 460.

[9] M. Saliba, J.-P. Correa-Baena, C. M. Wolff, M. Stolterfoht, N. Phung, S. Albrecht, D. Neher, A. Abate, *Chem. Mater.* **2018**, *30*, 4193.

[10] B. Li, D. Binks, G. Cao, J. Tian, *Small* **2019**, *15*, 1903613.

[11] A. Wakamiya, M. Endo, T. Sasamori, N. Tokitoh, Y. Ogomi, S. Hayase, Y. Murata, *Chem. Lett.* **2014**, *43*, 711.

[12] Y. Zhang, S. G. Kim, D. K. Lee, N. G. Park, *ChemSusChem* **2018**, *11*, 1813.

[13] a) Y. Zhang, S. Seo, S. Y. Lim, Y. Kim, S.-G. Kim, D.-K. Lee, S.-H. Lee, H. Shin, H. Cheong, N.-G. Park, *ACS Energy Lett.* **2019**, *5*, 360; b) M. Kim, G.-H. Kim, T. K. Lee, I. W. Choi, H. W. Choi, Y. Jo, Y. J. Yoon, J. W. Kim, J. Lee, D. Huh, H. Lee, S. K. Kwak, J. Y. Kim, D. S. Kim, *Joule* **2019**, *3*, 2179.

[14] H. J. Yen, P. W. Liang, C. C. Chueh, Z. Yang, A. K. Jen, H. L. Wang, *ACS Appl. Mater. Interfaces* **2016**, *8*, 14513.

[15] D. Prochowicz, P. Yadav, M. Saliba, M. Saski, S. M. Zakeeruddin, J. Lewinski, M. Gratzel, *ACS Appl. Mater. Interfaces* **2017**, *9*, 28418.

[16] J. H. Heo, S. H. Im, *Nanoscale* **2016**, *8*, 2554.

[17] B.-X. Chen, W.-G. Li, H.-S. Rao, Y.-F. Xu, D.-B. Kuang, C.-Y. Su, *Nano Energy* **2017**, *34*, 264.

[18] S. S. Mali, H. Kim, H. H. Kim, S. E. Shim, C. K. Hong, *Mater. Today* **2018**, *21*, 483.

[19] a) T. Baikie, N. S. Barrow, Y. Fang, P. J. Keenan, P. R. Slater, R. O. Piltz, M. Gutmann, S. G. Mhaisalkar, T. J. White, *J. Mater. Chem. A* **2015**, *3*, 9298; b) Q. Han, S. H. Bae, P. Sun, Y. T. Hsieh, Y. M. Yang, Y. S. Rim, H. Zhao, Q. Chen, W. Shi, G. Li, Y. Yang, *Adv. Mater.* **2016**, *28*, 2253.

[20] M. Xiao, F. Huang, W. Huang, Y. Dkhissi, Y. Zhu, J. Etheridge, A. Gray-Weale, U. Bach, Y. B. Cheng, L. Spiccia, *Angew Chem., Int. Ed. Engl.* **2014**, *53*, 9898.

[21] a) X. Liu, Y. Cheng, C. Liu, T. Zhang, N. Zhang, S. Zhang, J. Chen, Q. Xu, J. Ouyang, H. Gong, *Energy Environ. Sci.* **2019**, *12*, 1718; b) L. Jiang, J. Lu, S. R. Raga, J. Sun, X. Lin, W. Huang, F. Huang, U. Bach, Y.-B. Cheng, *Nano Energy* **2019**, *58*, 687.

[22] M. Stolterfoht, C. M. Wolff, Y. Amir, A. Paulke, L. Perdigón-Toro, P. Caprioglio, D. Neher, *Energy Environ. Sci.* **2017**, *10*, 1530.

[23] N. J. Jeon, H. Na, E. H. Jung, T.-Y. Yang, Y. G. Lee, G. Kim, H.-W. Shin, S. Il Seok, J. Lee, J. Seo, *Nat. Energy* **2018**, *3*, 682.

[24] a) D. Liu, W. Zhou, H. Tang, P. Fu, Z. Ning, *Sci. China Chem.* **2018**, *61*, 1278; b) P. Fassl, V. Lami, A. Bausch, Z. Wang, M. T. Klug, H. J. Snaith, Y. Vaynzof, *Energy Environ. Sci.* **2018**, *11*, 3380; c) P. Fassl, V. Lami, A. Bausch, Z. Wang, M. T. Klug, H. J. Snaith, Y. Vaynzof, *Energy Environ. Sci.* **2018**, *11*, 3380; d) J. Chang, H. Zhu, B. Li, F. H. Isikgor, Y. Hao, Q. Xu, J. Ouyang, *J. Mater. Chem. A* **2016**, *4*, 887.

[25] H. Tsai, W. Nie, Y.-H. Lin, J. C. Blancon, S. Tretiak, J. Even, G. Gupta, P. M. Ajayanand, A. D. Mohite, *Adv. Energy Mater.* **2017**, *7*, 1602159.

[26] a) A. R. Pascoe, Q. Gu, M. U. Rothmann, W. Li, Y. Zhang, A. D. Scully, X. Lin, L. Spiccia, U. Bach, Y.-B. Cheng, *Sci. China Mater.* **2017**, *60*, 617; b) X. Lian, J. Chen, M. Qin, Y. Zhang, S. Tian, X. Lu, G. Wu, H. Chen, *Angew. Chem., Int. Ed. Engl.* **2019**, *58*, 1.

[27] D. Bi, W. Tress, M. I. Dar, P. Gao, J. Luo, C. Renevier, K. Schenk, A. Abate, F. Giordano, J.-P. C. Baena, J.-D. Decoppet, S. M. Zakeeruddin, M. K. Nazeeruddin, M. Grätzel, A. Hagfeldt, *Sci. Adv.* **2016**, *2*, e1501170.

[28] M. Cai, N. Ishida, X. Li, X. Yang, T. Noda, Y. Wu, F. Xie, H. Naito, D. Fujita, L. Han, *Joule* **2017**, *2*, 296.

[29] Y. Wu, W. Chen, Y. Lin, B. Tu, X. Lan, Z. Wu, R. Liu, A. B. Djurišić, Z. B. He, *ACS Appl. Energy Mater.* **2018**, *1*, 3984.

[30] H. Tan, A. Jain, O. Voznyy, X. Lan, F. P. G. D. Arquer, J. Z. Fan, R. Quintero-Bermudez, M. Yuan, B. Zhang, Y. Zhao, F. Fan, P. Li, L. N. Quan, Y. Zhao, Z.-H. Lu, Z. Yang, S. Hoogland, E. H. Sargent, *Science* **2017**, *355*, 722.

[31] M. Stolterfoht, C. M. Wolff, J. A. Márquez, S. Zhang, C. J. Hages, D. Rothhardt, S. Albrecht, P. L. Burn, P. Meredith, T. Unold, D. Neher, *Nat. Energy* **2018**, *3*, 847.

[32] H. Min, G. Kim, M. J. Paik, S. Lee, W. S. Yang, M. Jung, S. I. Seok, *Adv. Energy Mater.* **2019**, *9*, 1803476.

[33] T. Wu, Y. Wang, X. Li, Y. Wu, X. Meng, D. Cui, X. Yang, L. Han, *Adv. Energy Mater.* **2019**, *9*, 1803766.

[34] D. Yang, X. Zhou, R. Yang, Z. Yang, W. Yu, X. Wang, C. Li, S. Liu, R. P. H. Chang, *Energy Environ. Sci.* **2016**, *9*, 3071.

[35] C. M. Wolff, F. Zu, A. Paulke, L. P. Toro, N. Koch, D. Neher, *Adv. Mater.* **2017**, *29*, 1700159.

[36] a) J. H. Kim, S. T. Williams, N. Cho, C.-C. Chueh, A. K.-Y. Jen, *Adv. Energy Mater.* **2015**, *5*, 1401229; b) Q. Wang, C. Bi, Y. Liu, Y. Deng, Y. Bai, Q. Dong, J. Huang, *Energy Environ. Sci.* **2017**, *10*, 516.

[37] E. H. Anaraki, A. Kermanpur, L. Steier, K. Domanski, T. Matsui, W. Tress, M. Saliba, A. Abate, M. Grätzel, A. Hagfeldt, J.-P. Correa-Baena, *Energy Environ. Sci.* **2016**, *9*, 3128.